J Nanostruct 16(4): 4577-4587, Autumn 2026

RESEARCH PAPER

Silicon-Modified ZnC/ZnO Nanocomposites: Synthesis, Characterization and Anticorrosion Performance

*Nada Saad Abd *, Saad Shahad Mohammed*

Department of Chemistry, College of Science, University of Thi-Qar, Thi-Qar 64001, Iraq

ARTICLE INFO

Article History:
Received 27 April 2026
Accepted 15 July 2026
Published 01 October 2026

Keywords:
Carbon nanocomposite
Corrosion inhibition
Green synthesis
Silicon modification
Stainless steel
Zinc oxide

ABSTRACT

A green and comparatively simple route was used to prepare a silicon-modified ZnC/ZnO nanocomposite, after which its capacity to protect stainless steel against acid attack was examined. Zinc nitrate hexahydrate served as the zinc source, a small quantity of silicon nanopowder was introduced as the modifier, and an aqueous extract of Ziziphus spina-christi (Sidr) leaves was employed at once as a reducing/capping agent and as the carbon precursor. Following precipitation under mildly alkaline conditions, the solid was calcined at 600°C under an argon atmosphere, a step that preserved a carbon-rich phase next to the oxide instead of burning it away. X-ray diffraction confirmed a well-crystallized hexagonal wurtzite ZnO together with reflections that belong to crystalline silicon, while the plant-derived carbon stayed largely amorphous. Field-emission scanning electron microscopy showed agglomerated, roughly spheroidal primary particles of about 36–64 nm that assembled into porous, cauliflower-like clusters; energy-dispersive spectroscopy detected only Zn, Si, C and O, in line with the intended composition. Thermogravimetric analysis pointed to good thermal stability, the total mass loss up to 900°C being only around 5.7%. Diffuse-reflectance spectra placed the near-band-edge absorption near 381 nm, equivalent to an optical band gap close to 3.2eV, with a tail extending into the visible. Tested in 0.5M H_2SO_4 by the weight-loss method, the composite behaved as a moderate inhibitor for 304 stainless steel; the inhibition efficiency increased with dose and with pH but decreased as the temperature and the immersion time were raised, which is consistent with a mainly physical adsorption mechanism.

How to cite this article
Saad Abd N., Mohammed S. Silicon-Modified ZnC/ZnO Nanocomposites: Synthesis, Characterization and Anticorrosion Performance. J Nanostruct, 2026; 16(4):4577-4587. DOI: 10.22052/JNS.2026.04.007

INTRODUCTION

Corrosion of metallic materials in acidic environments remains a persistent and costly problem for many industries, particularly in operations such as acid pickling, descaling and cleaning where sulfuric acid is widely used [1]. Even alloys that are normally regarded as resistant, like the austenitic 304 stainless steel, can suffer appreciable dissolution when the medium is strongly acidic. Among the various strategies developed to mitigate this damage, the use of inhibitors is still one of the most practical and economical options. Conventional synthetic inhibitors, such as gemini surfactants [2] and Schiff bases [3], have long been applied to limit the corrosion of steels in acidic solution, but over

* *Corresponding Author Email: nada.saad@utq.edu.iq*

the last decade attention has shifted noticeably towards inhibitors that are environmentally benign rather than toxic [4,5]. Plant extracts have attracted special interest in this regard, because the phytochemicals they contain, such as flavonoids, polyphenols, tannins and terpenoids, carry heteroatoms and aromatic systems that can adsorb on a metal surface and block the active sites where corrosion begins [5].

In parallel, zinc oxide has continued to be one of the most studied semiconductors owing to its wide band gap, large exciton binding energy, chemical and thermal stability, low cost and low toxicity [6]. The green, plant-mediated preparation of ZnO nanoparticles is now well documented, with the extract acting as a reducing and stabilizing medium that also tends to give finer, less aggregated particles [7]. ZnO and ZnO-based materials have, moreover, shown promise as corrosion inhibitors: green-synthesized ZnO nanoparticles and several ZnO nanocomposites have been reported to retard the corrosion of steels in acidic media, often by forming a barrier film at the interface [8,9,10]. A recurring observation is that combining ZnO with a second phase, whether a polymer, a carbon material or another oxide, improves the inhibition relative to the bare oxide [11,12].

The present work was built around these ideas. An aqueous extract of Ziziphus spina-christi (locally known as Sidr), a tree abundant in Iraq and already reported as a route to wurtzite ZnO nanoparticles [13,14], was used here not only as the green agent but also as a source of carbon, since calcination under argon preserves the organic-derived carbon instead of oxidizing it. A small amount of silicon nanopowder was added as a modifier, with the aim of tuning the structural and optical behaviour of the product, an approach loosely inspired by earlier ZnO–silica systems [15]. The resulting silicon-modified ZnC/ZnO nanocomposite was characterized by XRD, FESEM, EDS, TGA and DRS, and its performance as a corrosion inhibitor for 304 stainless steel in 0.5 M H_2SO_4 was then evaluated by weight loss as a function of immersion time, temperature, inhibitor dose and pH.

MATERIALS AND METHODS

Materials

Zinc nitrate hexahydrate ($Zn(NO_3)_2{\cdot}6H_2O$), silicon nanopowder, sodium hydroxide (NaOH), ethanol (C_2H_5OH) and sulfuric acid (H_2SO_4) were purchased from Sigma-Aldrich. All chemicals were used as received, without any further purification. Deionized water was used throughout for preparing and diluting the solutions and samples. Fresh leaves of Ziziphus spina-christi were collected in Dhi Qar governorate, Iraq, for the preparation of the plant extract.

Preparation of Ziziphus spina-christi leaf aqueous extract

Leaves of Ziziphus spina-christi (Sidr) were gathered from trees in the Al-Gharraf District, Dhi Qar, Iraq. They were first washed with tap water and then with deionized water to remove dust and impurities, after which they were air-dried in the shade at room temperature for two weeks and ground in a high-speed electric grinder to a fine powder. The aqueous extract was prepared by adding 10 g of the leaf powder to 100 mL of deionized water in a 250 mL flask and heating the mixture at 50 °C for 2 h under continuous stirring. The extract was filtered first through cheesecloth and then through Whatman No. 1 filter paper, and the filtrate was centrifuged at 5000 rpm for 15 min to obtain a clear supernatant. The extract was kept in dark glass bottles at 4 °C until use.

Synthesis of the silicon-modified ZnC/ZnO nanocomposite

Zinc nitrate hexahydrate was used as the zinc-ion source. 5 g of $Zn(NO_3)_2{\cdot}6H_2O$ was dissolved in 100 mL of deionized water in a 250 mL flask. After complete dissolution, 0.15 g of silicon nanopowder was added and the flask was sonicated for 30 min to disperse the silicon. 70 mL of the plant extract, prepared 3 h earlier, was then added, and the solution was homogenized on a magnetic stirrer. The pH was adjusted to 8–10 by dropwise addition of 1 M NaOH at 60–80 °C, on which a green solution formed. Stirring and heating were maintained for 4 h to ensure complete precipitation and homogeneity. The suspension was centrifuged at 8000 rpm for 15 min, and the precipitate was separated and washed three times with ethanol and deionized water to remove residual impurities and by-products. The solid was dried in an oven at 100 °C, ground to a fine powder, and finally calcined under an argon atmosphere at 600 °C for 3 h.

Characterization

The crystal structure and phases of the nanocomposite were determined by X-ray

diffraction (XRD; Philips PW1730, Netherlands) using Cu Kα radiation (λ = 1.541 Å) over a 2θ range of 10°–80°. Particle size and surface morphology were examined by field-emission scanning electron microscopy (FESEM; Inspect F50, Netherlands). The elemental composition was analysed by energy-dispersive X-ray spectroscopy (EDS; Thermo Scientific Axia ChemiSEM, Netherlands). Fourier-transform infrared (FTIR) spectra were recorded on a Shimadzu FTIR Affinity spectrometer (Japan). Thermal stability and decomposition behaviour were evaluated by thermogravimetric analysis (TGA; HZ2329 Thermal Analysis, China). The optical band gap and absorption properties were obtained from diffuse-reflectance spectroscopy (DRS; AvaLight-DH-S-BAL, Netherlands).

Corrosion test

Stainless steel sheets of type 304 were used as the substrate. Their nominal composition was about 18–20% chromium and 8–10.5% nickel, with small amounts of carbon (≤0.08%), manganese and silicon, the balance being iron. Before each run the coupons were prepared, degreased, cleaned, rinsed with distilled water and dried. The silicon-modified ZnC/ZnO nanocomposite was used as the inhibitor. The test solution was 0.5 M H_2SO_4 prepared with distilled water, and its pH was adjusted, when needed, with 0.5 M NaOH. This acid concentration was chosen because it is commonly encountered in industrial pickling. Measurements were carried out in unstirred, naturally aerated solution at 298, 308 and 313 K, using inhibitor amounts of 0.5, 1.0, 1.5 and 2.0 g. Each coupon was weighed before immersion and then exposed to the solution with or without the inhibitor; every experiment was repeated three times. After the selected immersion times the coupons were removed, rinsed with distilled water, cleaned with ethanol, dried with acetone and re-weighed, and the weight loss was taken as the difference between the initial and final masses.

The corrosion rate (CR) was calculated from:

$$CR = (87.6 \times W) / (D \times A \times T)$$

where W is the weight loss, D the density of the coupon, A the exposed surface area and T the immersion time. The surface coverage (θ) and the inhibition efficiency (IE%) were obtained from:

$$\theta = (CR_o - CR) / CR_o$$

$$IE\% = [(CR_o - CR) / CR_o] \times 100$$

where CR_o is the corrosion rate of the blank (without inhibitor) and CR the corrosion rate in the presence of the inhibitor.

RESULTS AND DISCUSSION

X-ray diffraction (XRD)

The diffraction pattern of the prepared powder (Fig. 1) is dominated by a set of sharp, intense reflections that match the hexagonal wurtzite structure of ZnO (JCPDS card no. 36-1451). The main peaks appear at 2θ ≈ 31.85°, 34.51° and 36.36°, which are assigned to the (100), (002) and (101) planes respectively, with the (101) reflection being the strongest, exactly as expected for well-crystallized wurtzite ZnO. Additional ZnO reflections were resolved at about 47.7° (102), 56.6° (110), 62.9° (103), 68.0° (112) and 69.2° (201), confirming the phase assignment. The sharpness and intensity of these peaks indicate that the oxide is highly crystalline. The lattice parameters refined from the (100) and (002) reflections were a ≈ 3.241 Å and c ≈ 5.193 Å, giving a c/a ratio of 1.602, in close agreement with the accepted values for wurtzite ZnO and with green-synthesized ZnO obtained from Ziziphus extracts in earlier reports [14,16].

A further reflection that does not belong to ZnO was observed at 2θ ≈ 28.5° (d ≈ 3.13 Å), accompanied by weaker companions near 47.4° and 56.2°. These positions correspond to the (111), (220) and (311) planes of cubic crystalline silicon, and their presence is consistent with retention of the added silicon nanopowder, which is not oxidized during calcination under the inert argon atmosphere. No distinct reflections of crystalline silica or zinc silicate were detected, suggesting that the silicon remains essentially as elemental Si rather than reacting extensively with the oxide under the conditions used. The carbon introduced through the plant extract did not give sharp peaks, which implies that it is mainly amorphous and contributes only to the diffuse background; a comparable behaviour has been noted for ZnO–biomass and carbon–ZnO composites prepared by similar inert-atmosphere routes [17,18]. The mean crystallite size, estimated from the Debye–Scherrer equation applied to the principal ZnO reflections, was on the order of 40 nm, which agrees reasonably with the primary particle sizes

seen by FESEM (Section 3.2) and with the ~38 nm value reported for ZnO obtained from Sidr leaf extract [14].

Surface morphology (FESEM)

The FESEM micrographs, collected at magnifications ranging from 4,000× to about 97,000× (Fig. 2), reveal a hierarchical, agglomerated microstructure. At low magnification the powder appears as irregular micron-scale aggregates separated by open, macroporous channels, whereas at higher magnification these aggregates

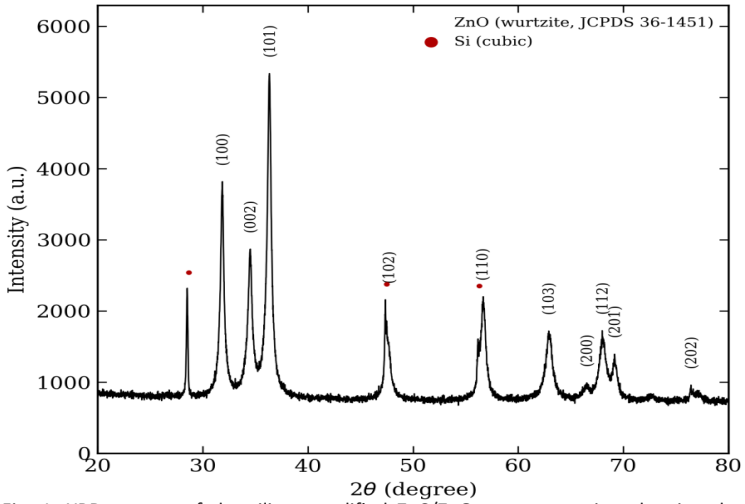

Fig. 1. XRD pattern of the silicon-modified ZnC/ZnO nanocomposite, showing the indexed wurtzite ZnO reflections (JCPDS 36-1451) together with the cubic Si reflections.

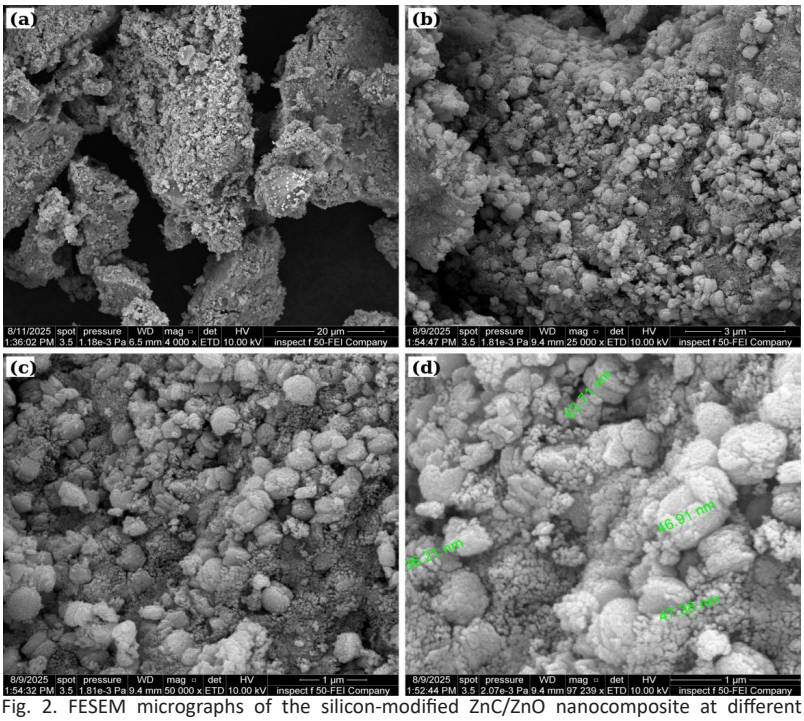

Fig. 2. FESEM micrographs of the silicon-modified ZnC/ZnO nanocomposite at different magnifications (panels a–d), with representative primary particle sizes indicated; the images illustrate the porous, agglomerated nanostructure.

are clearly resolved into much smaller primary particles. The primary particles are mostly equiaxed to slightly elongated and rather closely packed, and direct measurements on the images gave diameters in the range of about 36–64 nm (with representative values near 36, 47 and 64 nm). These primary units cluster into porous, cauliflower-like secondary structures, so that the overall material combines nanoscale building blocks with a relatively open, high-surface texture. Such a porous and granular morphology, which resembles that reported for other green-synthesized ZnO nanoparticles [12], is generally favourable for an inhibitor because it offers a large contact area and many sites able to interact with the metal surface. The particle sizes obtained from the images are consistent with the crystallite size estimated from XRD, indicating that each primary particle is composed of only one or a few crystallites.

Elemental composition (EDS)

The EDS spectrum (Fig. 3) and the corresponding quantitative results (Table 1) show that the nanocomposite is composed only of zinc, silicon, carbon and oxygen, with no other detectable element. Zinc is clearly the dominant constituent (about 74.8 wt% and 44.5 at%), as expected for a ZnO-rich material, and is accompanied by a substantial silicon signal (11.4 wt%, 15.8 at%) that confirms the incorporation of the added silicon modifier and is fully consistent with the crystalline Si reflections seen by XRD. The carbon content (7.7 wt%, 24.9 at%) reflects the bio-derived carbon retained from the Sidr extract after calcination under argon, rather than mere surface contamination, while the oxygen (6.1 wt%, 14.8 at%) is associated mainly with the oxide. The apparent oxygen-to-zinc ratio is lower than the 1:1 expected for stoichiometric ZnO; this is partly a known limitation of EDS for light elements such as oxygen and carbon, and partly a reflection of the composite nature of the sample, in which a large fraction of the signal originates from the silicon and carbon phases. A broadly similar elemental distribution, with comparable carbon, oxygen and zinc fractions, has been reported for carbon-supported ZnO-based composites [19].

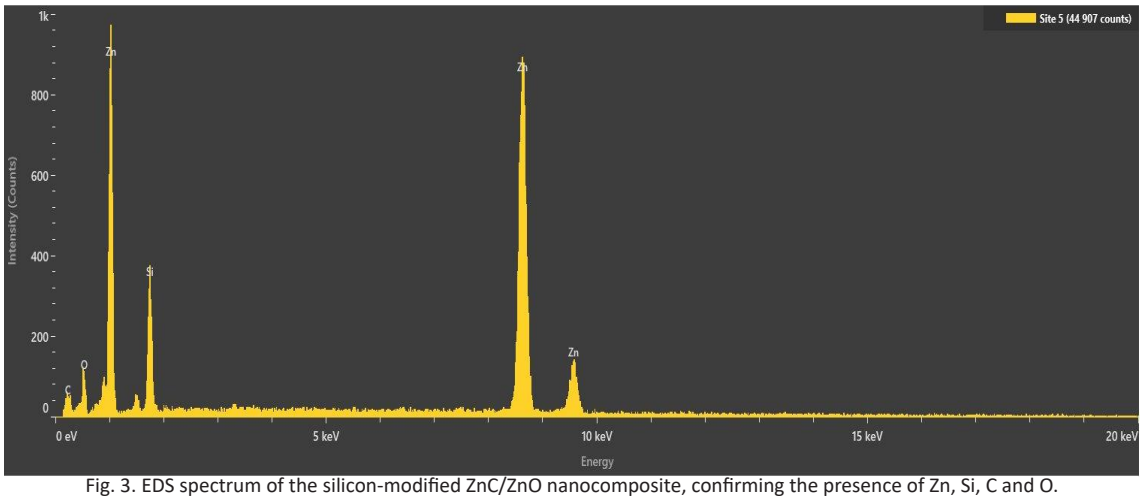

Fig. 3. EDS spectrum of the silicon-modified ZnC/ZnO nanocomposite, confirming the presence of Zn, Si, C and O.

Table 1. Elemental composition of the silicon-modified ZnC/ZnO nanocomposite obtained from EDS analysis.

Element	Atomic %	Atomic % Error	Weight %	Weight % Error
C	24.9	2.2	7.7	0.7
O	14.8	0.9	6.1	0.4
Si	15.8	0.3	11.4	0.2
Zn	44.5	0.7	74.8	1.1

Thermal behaviour (TGA/DTG/DSC)

The thermal response of the nanocomposite was followed from room temperature up to about 900 °C (Fig. 4). The overall mass loss was small, only about 5.7% of the initial mass, and the residue at the end of the run amounted to roughly 94.4%, which already points to a thermally robust material dominated by the inorganic ZnO and Si phases. Several overlapping steps can be distinguished. A minor loss below ~160 °C (about 0.3%) is attributed to the release of physisorbed moisture. A more pronounced loss between roughly 175 and 305 °C, made up of two close steps totalling about 3.3%, is assigned to the removal of more strongly held water together with the decomposition of the bio-derived carbon and residual organic fragments left from the plant extract. Smaller losses between about 358 and 460 °C (around 0.9% in total) complete the decomposition, after which the curve flattens into a stable plateau up to 900 °C, confirming that the remaining oxide/silicon framework is essentially unchanged at high

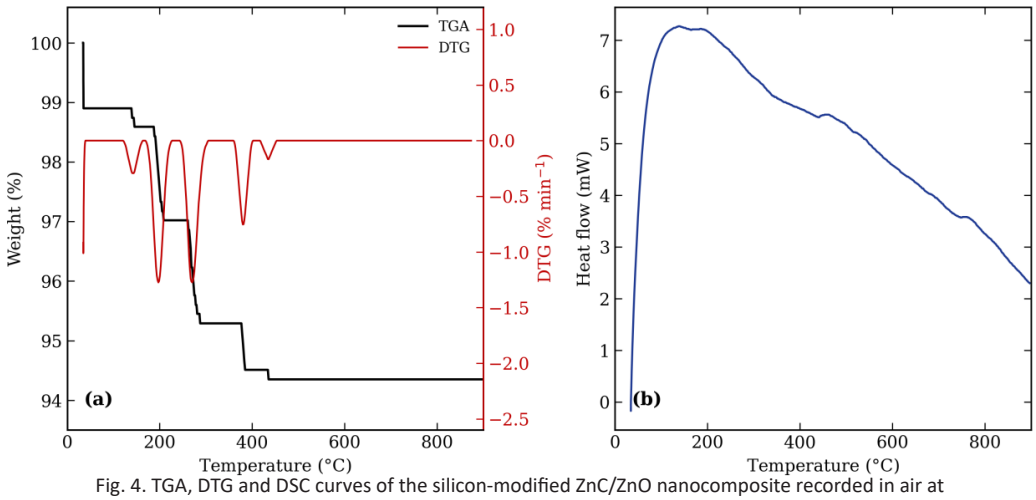

Fig. 4. TGA, DTG and DSC curves of the silicon-modified ZnC/ZnO nanocomposite recorded in air at

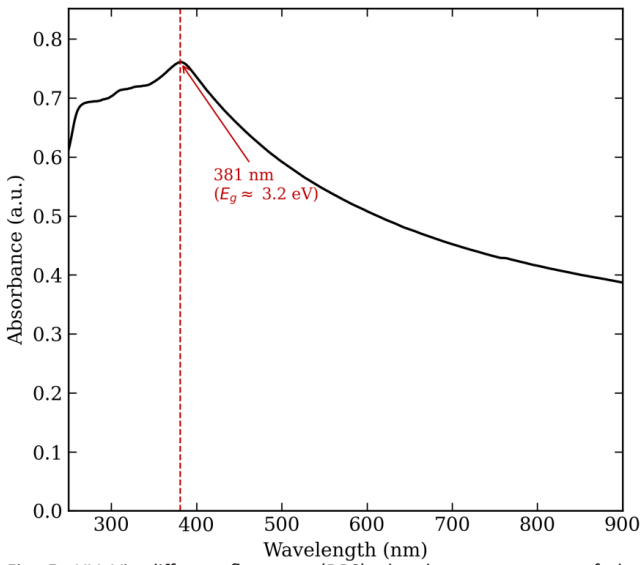

Fig. 5. UV–Vis diffuse-reflectance (DRS) absorbance spectrum of the silicon-modified ZnC/ZnO nanocomposite; the near-band-edge absorption at ~381 nm corresponds to an optical band gap of about 3.2 eV, with a broad tail extending into the visible region.

temperature. The heat-flow (DSC) signal changed slope in the same low-temperature region (around 140 °C), in line with the dehydration step seen in the TGA/DTG curves, with only weak thermal events at higher temperature. This high stability and modest weight loss are in keeping with what has been reported for ZnO–biomass and carbon/ZnO systems, where the inorganic component dominates the residual mass [17,18].

Optical properties (DRS)

The diffuse-reflectance spectrum (Fig. 5) displays a clear absorption maximum near 381 nm, which corresponds to the characteristic near-band-edge absorption of ZnO and reflects the electronic transition across its band gap. Converting this edge wavelength to energy (1240/381) gives a value close to 3.2 eV, in good agreement with the band gap usually quoted for ZnO and with green-synthesized ZnO in the literature. It should be noted that the absorption does not fall to zero on the long-wavelength side; instead a broad, almost featureless tail extends well into the visible and near-infrared, so that the powder still absorbs strongly (absorbance ~0.4–0.5) even at 600–900 nm. This behaviour is attributed to the silicon and, especially, the carbon phases of the composite, both of which absorb across the whole visible range and give the material its dark appearance. Because of this strong background absorption, a conventional Tauc extrapolation did not yield a well-defined linear region, and the band gap was therefore estimated from the position of the near-band-edge feature rather than from a Tauc intercept; a similar broadening and an apparent extension of the absorption have been reported when ZnO is combined with silica or carbon phases [15,20]. A weaker absorption in the deep ultraviolet (~213 nm) is associated with higher-energy transitions.

FTIR analysis

FTIR spectroscopy was used to probe the functional groups present in the nanocomposite, and the recorded spectrum is shown in Fig. 6. The broad band centred at 3433 and 3394 cm^{-1} is assigned to O–H stretching of adsorbed water and surface hydroxyl groups, together with residual O–H of the plant-derived carbon [17,19]. The strong, sharp absorption at 1450 cm^{-1} is attributed to aromatic C=C and C–O vibrations together with carbonate (CO_3^{2-}) species associated with the bio-derived carbon retained after calcination [17,19]. The bands at 1141 and 1057 cm^{-1} lie in the region characteristic of Si–O–Si and Si–O stretching and confirm the presence of the silicon modifier, while the weaker feature near 879 cm^{-1} is consistent with Si–O bending and out-of-plane carbonate modes [15,20]. The intense absorption at 486 cm^{-1} corresponds to the Zn–O stretching vibration of the wurtzite lattice, in agreement with the XRD results and with the values reported for green-synthesized ZnO and ZnO–SiO_2 systems [19,20]. Taken together, the FTIR bands confirm the

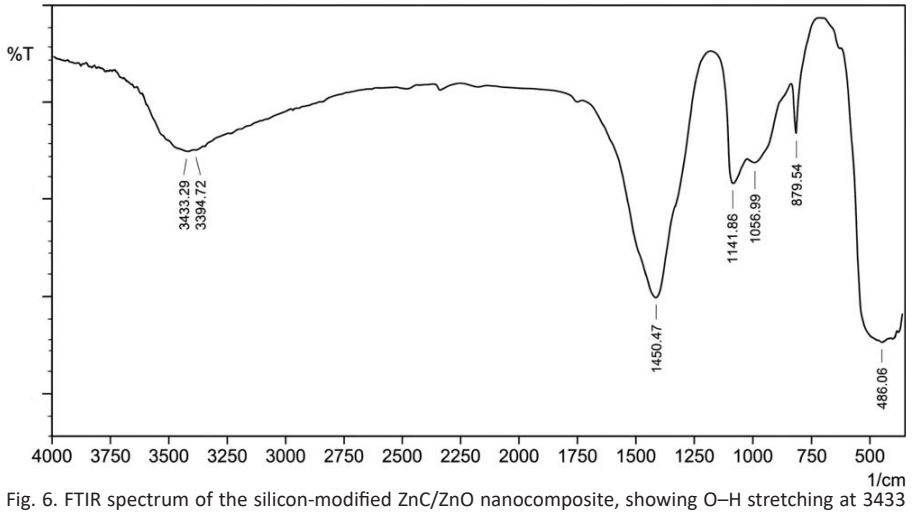

Fig. 6. FTIR spectrum of the silicon-modified ZnC/ZnO nanocomposite, showing O–H stretching at 3433 and 3394 cm^{-1}, the C=C/carbonate band of the bio-derived carbon at 1450 cm^{-1}, Si–O(–Si) vibrations at 1141, 1057 and 879 cm^{-1}, and the characteristic Zn–O lattice stretching at 486 cm^{-1}.

coexistence of ZnO, a silicon-containing phase and a residual bio-carbon component, fully consistent with the XRD, EDS and TGA findings.

Anti-corrosion performance

The ability of the silicon-modified ZnC/ZnO nanocomposite to inhibit the corrosion of 304 stainless steel in 0.5 M H_2SO_4 was evaluated by the weight-loss method, examining in turn the effects of immersion time, temperature, inhibitor dose and pH (Fig. 7).

Effect of immersion time

Fig. 7a summarizes the effect of immersion time at 298 K. The corrosion rate increased with time in both the inhibited and the blank solutions, which indicates progressive dissolution of the metal as the exposure is prolonged. At every time studied, however, the corrosion rate in the presence of 0.5 g of inhibitor stayed below that of the blank, confirming the protective action of the nanocomposite. The highest inhibition efficiency, about 50.5%, was reached after 10 h, suggesting that the inhibitor particles adsorb relatively quickly and form an effective protective film early on. As the immersion time was extended to 40 h the efficiency fell gradually to roughly 23%, most likely because of partial desorption, thinning or deterioration of the adsorbed layer in the aggressive acidic medium. Even so, the inhibited system retained lower corrosion rates than the blank throughout, so the material continues to act as a surface barrier against the acid.

Effect of temperature

The influence of temperature, measured after 10 h of immersion, is shown in Fig. 7b. Raising the temperature accelerated the corrosion markedly in both solutions: with 0.5 g of inhibitor the corrosion rate increased from 0.238 at 298 K to 3.808 ($\times 10^{-3}$ mm/year) at 313 K, while the blank rose in a similar fashion. This is the usual consequence of

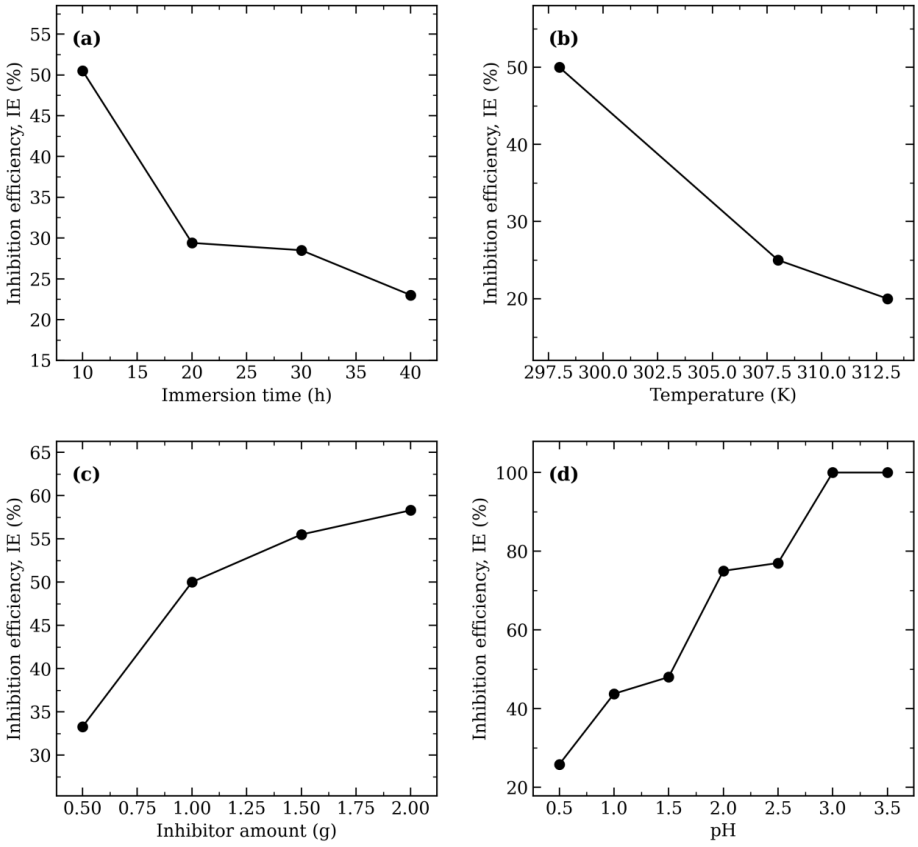

Fig. 7. Inhibition efficiency (IE%) of the inhibitor for 304 stainless steel in 0.5 M H_2SO_4 as a function of (a) immersion time at 298 K, (b) temperature after 10 h, (c) inhibitor amount at 298 K after 10 h, and (d) pH at 298 K after 10 h.

a faster electrochemical reaction and easier metal dissolution at higher temperature. The inhibition efficiency, in turn, dropped from about 50% at 298 K to roughly 20% at 313 K. Such a decrease of efficiency with rising temperature is generally taken as evidence that the inhibitor is held mostly by physical (electrostatic) adsorption, which weakens as the temperature increases and the adsorbed species begin to desorb. A comparable decline of inhibition efficiency with rising temperature has been reported for organic inhibitors of AISI steel in sulfuric acid, where the effect was likewise attributed to weakening of the physically adsorbed film [2]. Despite this, the inhibited solution still corroded more slowly than the blank at all three temperatures, so the nanocomposite remained effective, if less so, under hotter conditions.

Effect of inhibitor dose

Fig. 7c shows how the amount of inhibitor affects the protection at 298 K after 10 h. The inhibition efficiency increased steadily with dose, from about 33.3% at 0.5 g to roughly 58.3% at 2.0 g. The improvement is consistent with the idea that a larger quantity of the nanocomposite provides more active adsorption sites and thus a higher surface coverage, building a more complete protective barrier on the steel and reducing direct contact between the metal and the acid. In this way both the anodic dissolution of the metal and the cathodic hydrogen-evolution reaction are suppressed. All inhibited systems corroded less than the blank, and the best protection was obtained at the highest dose studied.

Effect of pH

The role of acidity is presented in Fig. 7d. The corrosion rate decreased sharply as the pH was raised, in both the inhibited and the blank solutions. With 0.5 g of inhibitor the corrosion rate dropped from a high value at pH 0.5 to essentially zero at pH 3.0 and 3.5, meaning that no measurable corrosion remained under these milder conditions. Correspondingly, the inhibition efficiency rose from about 25.8% at pH 0.5 to 77% at pH 2.5 and reached 100% at pH 3.0 and 3.5. The trend shows that the nanocomposite is far more effective in less acidic media, where the concentration of aggressive hydrogen ions is lower and the adsorption of the inhibitor species on the steel is favoured. The blank also corroded less as the pH increased, confirming the strong influence of acidity on metal dissolution, but at every pH the inhibited system performed better. On the whole, then, increasing the pH improved both the intrinsic corrosion resistance and the inhibitor performance, and the material appears particularly suited to moderately acidic conditions.

Inhibition mechanism and comparison with previous work

Taken together, the four sets of measurements point to a mainly physical adsorption mechanism. The efficiency improves with inhibitor dose, which

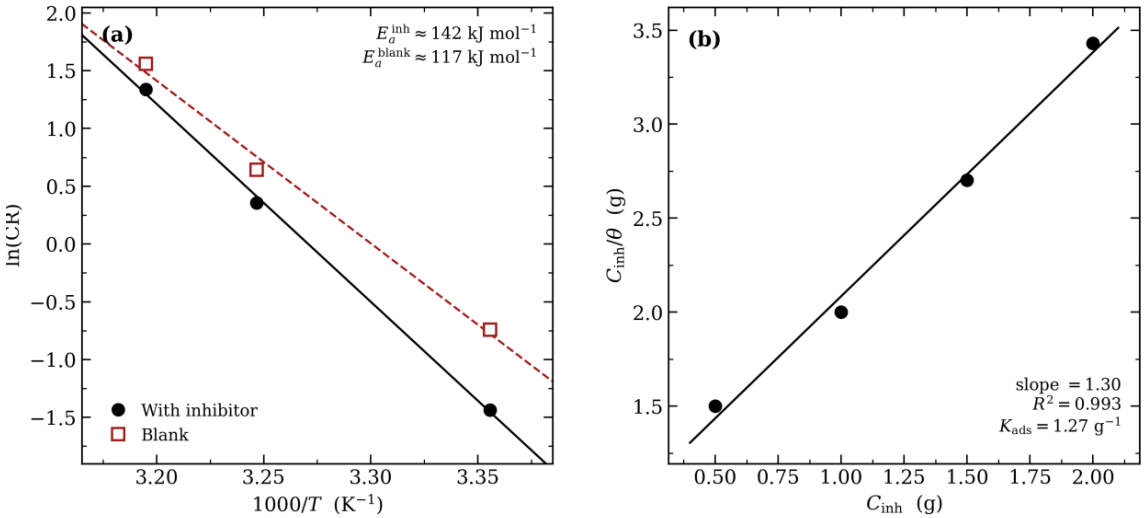

Fig. 8. (a) Arrhenius plots (ln CR versus 1000/T) for 304 stainless steel in 0.5 M H_2SO_4 with and without the inhibitor, used to estimate the apparent activation energy; (b) Langmuir adsorption isotherm (C/θ versus C) for the inhibitor at 298 K.

is the expected signature of increasing surface coverage as more of the nanocomposite adsorbs on the steel, and it improves as the medium becomes less acidic. In contrast, the efficiency falls when either the temperature or the immersion time is increased, both of which are typical of physisorbed layers that desorb or thin out under more demanding conditions [4,5]. The protective action itself is best understood as the formation of an adsorbed film that physically separates the metal from the corrosive solution and blocks active sites, thereby slowing both the anodic and the cathodic partial reactions; ZnO and ZnO-based nanocomposites are known to act in this barrier-type manner [10,11,12]. The porous, high-area morphology revealed by FESEM is likely to assist this process by increasing the number of contact points with the surface.

These trends were also examined quantitatively. An Arrhenius treatment of the corrosion rate (Fig. 8a) gave an apparent activation energy of about 142 kJ mol^{-1} in the presence of the inhibitor, higher than the ≈117 kJ mol^{-1} obtained for the blank; this increase in activation energy on adding the inhibitor is consistent with a predominantly physical (electrostatic) adsorption, in which the adsorbed film raises the energy barrier to metal dissolution. The variation of the surface coverage with inhibitor amount was well described by the Langmuir adsorption isotherm (Fig. 8b): the plot of C/θ against C was linear ($R^2 \approx 0.99$) with a slope close to unity, pointing to monolayer adsorption of the nanocomposite on the steel surface.

In terms of absolute performance, the present material is a moderate inhibitor: the best efficiencies in strongly acidic 0.5 M H_2SO_4 were around 50–58%, rising to complete protection only as the pH approached 3. This is lower than some of the very high efficiencies (often 90–95%) reported for ZnO nanoparticles and ZnO–polymer composites in hydrochloric acid media [9,11,12], or for synthetic organic inhibitors such as gemini surfactants and Schiff bases applied to steel in acidic media [2,3], but a direct comparison is not entirely fair, because those studies used different metals (mostly mild or pipeline steels rather than the more resistant 304 stainless steel), a different acid, and in several cases electrochemical methods that probe a different time scale. The fact that a green, plant-derived nanocomposite can still appreciably retard the corrosion of stainless steel in sulfuric acid, and can suppress it completely under mildly acidic conditions, is nonetheless encouraging and suggests that further tuning of the silicon and carbon contents could improve the protection.

CONCLUSION

A silicon-modified ZnC/ZnO nanocomposite was successfully prepared by a green route in which an aqueous extract of Ziziphus spina-christi leaves acted both as a reducing and capping agent and as a carbon source, with silicon nanopowder added as a modifier and the product calcined under argon. XRD confirmed a highly crystalline wurtzite ZnO together with crystalline silicon, while the plant-derived carbon remained amorphous, so that the material is best described as ZnO nanocrystals combined with silicon and a bio-carbon phase. FESEM showed porous aggregates built from primary particles of about 36–64 nm, EDS confirmed the Zn, Si, C and O composition, and TGA demonstrated good thermal stability with only ~5.7% mass loss up to 900 °C. The optical study placed the band gap near 3.2 eV with absorption extended into the visible. As a corrosion inhibitor for 304 stainless steel in 0.5 M H_2SO_4, the nanocomposite was moderately effective; the efficiency increased with dose and pH but decreased with temperature and time, behaviour that is consistent with predominantly physical adsorption and the formation of a protective surface film. The results indicate that green-synthesized, silicon-modified ZnC/ZnO is a promising and environmentally friendly candidate for corrosion protection, and that its performance could be further improved by optimizing the composition.

CONFLICT OF INTEREST

The authors declare that there is no conflict of interests regarding the publication of this manuscript.

REFERENCES

1. Shathani P, Ogunmuyiwa EN, Obadele BA, Oladijo OP. Plant leaf extracts as green corrosion inhibitors of steel in acidic and seawater environments: a review. Environmental Science and Pollution Research. 2025;32(51):28954-28975.
2. Jerri Meften M. Gemini Surfactant Performance Evaluation as Inhibitive action of PAPM for Treatment of AISI steel Corrosion and Studying Temperatures Influence in Acidic Medium. University of Thi-Qar Journal of Science. 2019;7(1):103-112.
3. Synthesis and characterization of Novel Schiff bases and evaluation of Corrosion inhibitors and biological activity.

University of Thi-Qar Journal of Science. 2019.
4. Fazal BR, Becker T, Kinsella B, Lepkova K. A review of plant extracts as green corrosion inhibitors for CO2 corrosion of carbon steel. npj Materials Degradation. 2022;6(1).
5. R. Holla B, Mahesh R, Manjunath HR, Anjanapura VR. Plant extracts as green corrosion inhibitors for different kinds of steel: A review. Heliyon. 2024;10(14):e33748.
6. Biogenic Synthesis of Zinc Oxide Nanoparticles Mediated by the Extract of Terminalia catappa Fruit Pericarp and Its Multifaceted Applications. American Chemical Society (ACS).
7. Jayaseelan E, Nixon PD, Joseph. P B, Asir Gnanaraj M, Parameswari K, Ananthi N. Role OF KIT-6 on the fungicide and pesticide activities of zinc, copper and magnesium oxide nanoparticles prepared using Camellia sinensis extract (tea plant) through green synthesis. Nano-Structures and Nano-Objects. 2024;38:101119.
8. Dalmaz A, Kasımfırtına E, Sivrikaya Özak S. Green synthesis of ZnO nanoparticles using Laurus nobilis L. extract and investigation of corrosion inhibition properties of DES-based nanofluids. Journal of the Iranian Chemical Society. 2024;21(4):1101-1112.
9. Yadav A, Kumar H, Kumar P, Rani G, Maken S. Syzygium cumini leaf extract mediated green synthesis of ZnO nanoparticles: A sustained release for anticancer, antimicrobial, antioxidant, and anti-corrosive applications. J Mol Struct. 2025;1325:141017.
10. Quadri TW, Olasunkanmi LO, Fayemi OE, Solomon MM, Ebenso EE. Zinc Oxide Nanocomposites of Selected Polymers: Synthesis, Characterization, and Corrosion Inhibition Studies on Mild Steel in HCl Solution. ACS Omega. 2017;2(11):8421-8437.
11. Bairagi H, Vashishth P, Sehrawat R, Shukla SK, Mangla B. Impact of novel ZnO/PAA nanocomposite as corrosion inhibitor on mild steel in 5% HCl. Materials Chemistry and Physics. 2024;315:128958.
12. Bounedjar N, Ferhat MF, Toukal L, Messai R. Non thermal plasma synthesis of ZnO nanoparticles and their corrosion inhibition activity on XC70 mild steel pipeline in 1 M HCl acidic medium. Materials Chemistry and Physics. 2024;311:128555.
13. Shnawa BH, Jalil PJ, Al-Ezzi A, Mhamedsharif RM, Mohammed DA, Biro DM, et al. Evaluation of antimicrobial and antioxidant activity of zinc oxide nanoparticles biosynthesized with Ziziphus spina-christi leaf extracts. Journal of Environmental Science and Health, Part C. 2023;42(2):93-108.
14. El-Sawaf AK, El-Moslamy SH, Kamoun EA, Hossain K. Green synthesis of trimetallic CuO/Ag/ZnO nanocomposite using Ziziphus spina-christi plant extract: characterization, statistically experimental designs, and antimicrobial assessment. Sci Rep. 2024;14(1).
15. Rahmat Fi, Fen YW, Anuar MF, Omar NAS, Zaid MHM, Matori KA, et al. Synthesis and Characterization of ZnO-SiO2 Composite Using Oil Palm Empty Fruit Bunch as a Potential Silica Source. Molecules. 2021;26(4):1061.
16. Alharthi MN, Ismail I, Bellucci S, Salam MA. Green synthesis of zinc oxide nanoparticles by Ziziphus jujuba leaves extract: Environmental application, kinetic and thermodynamic studies. Journal of Physics and Chemistry of Solids. 2021;158:110237.
17. Akpomie KG, Conradie J. Synthesis, characterization, and regeneration of an inorganic–organic nanocomposite (ZnO@biomass) and its application in the capture of cationic dye. Sci Rep. 2020;10(1).
18. Wei X, Deng Y, Hu X, Zhao J, Wei H, Yang Z, et al. Biomass derived fibrous porous carbon loaded zinc oxide nanoparticles as high-performance anode materials for lithium ion batteries. Journal of Energy Storage. 2023;70:107854.
19. Cinnathambi Subramani M, Kandasamy B, Budiman I, Subyakto S, Chitraningrum N, Widyaningrum BA, et al. Synthesis and characterization of bamboo stem porous activated carbon/zinc oxide/copper oxide (BSPAC/ZnO/CuO) ternary nanocomposite for their biological activities. Biomass Conversion and Biorefinery. 2026;16(5).
20. Babu KS, Reddy AR, Reddy KV. Controlling the size and optical properties of ZnO nanoparticles by capping with SiO_2. Mater Res Bull. 2014;49:537-543.